Removal of carbon deposits on χ-Fe5C2 Fischer–Tropsch catalysts

Li, Shiyue; Pestman, Robert; Dugulan, A. Iulian; Men, Zhuowu; Wang, Peng; Hensen, Emiel J.M.

DOI
10.1016/j.jcat.2025.116030

Publication date
2025

Document Version
Final published version

Published in
Journal of Catalysis

Journal of Catalysis 445 (2025) 116030

Contents lists available at ScienceDirect

Journal of Catalysis

journal homepage: www.elsevier.com/locate/jcat

Removal of carbon deposits on χ-Fe_5C_2 Fischer–Tropsch catalysts

Shiyue Li [a], Robert Pestman [a], A. Iulian Dugulan [b], Zhuowu Men [c], Peng Wang [a,c,*], Emiel J.M. Hensen [a,*]

[a] Laboratory of Inorganic Materials and Catalysis, Department of Chemical Engineering and Chemistry, Eindhoven University of Technology, P.O. Box 513, 5600 MB Eindhoven, the Netherlands

[b] Fundamental Aspects of Materials and Energy Group, Delft University of Technology, 2629 JB Delft, the Netherlands

[c] National Institute of Clean-and-Low-Carbon Energy, Future Science & Technology City, Changping District, Beijing 102211, People's Republic of China

ARTICLE INFO

Keywords:
Fischer–Tropsch synthesis
Carbon removal
Induction period
Regeneration
Iron carbide

ABSTRACT

The removal of carbon deposits from carburized Fe-based Fischer–Tropsch catalysts is a critical aspect of their performance. In this study, a method is presented to remove carbon deposits from freshly prepared χ-Fe_5C_2. The method involves successive passivation and reduction steps, which do not affect the bulk structure of the χ-Fe_5C_2 catalyst. The passivation step transforms the carbonaceous deposits from a graphitic structure to a disordered oxygen-functionalized structure, facilitating its removal by a reduction step in hydrogen. This results in a higher initial activity of the catalyst and substantially shortens the induction period observed without such pretreatment. The findings underscore the possibility of improving catalytic performance of Fe-carbides by changing the structure and reactivity of carbonaceous deposits.

1. Introduction

Fischer–Tropsch (FT) synthesis has grown in importance in the last two decades, becoming a significant technology for converting natural gas and coal into liquid fuels and chemicals via synthesis gas (a mixture of CO and H_2) [1]. Although Co and Ru are well suited for FT synthesis, Fe-based catalysts are often preferred because of their lower cost, higher tolerance to sulfur, and ability to cope with synthesis gas with low H_2/CO ratios [2]. During or before the reaction, Fe-based catalysts are transformed into Fe-carbides. The co-existence of several of these Fe-bearing phases, including metallic Fe and Fe-oxides, makes it difficult to determine accurate structure-performance relationships. Among Fe-carbide phases, χ-Fe_5C_2 (Hägg carbide) is the most stable and active phase under typical FT conditions [3–5]. χ-Fe_5C_2 can be obtained in various ways. Commercial Fe-based catalysts are typically prepared by reducing and carburizing a precipitated Fe_2O_3 precursor [6,7]. The carburization step is usually done in a synthesis gas mixture, resulting in a mixture of Fe phases, which most often include χ-Fe_5C_2. Yang et al. synthesized χ-Fe_5C_2 nanoparticles through a one-pot wet-chemical method [3]. De Smit et al. investigated the stability of ε-, χ-, and θ-Fe-carbides as a function of the composition of the carburizing gas mixture and the carburization temperature [8]. Compared to ε- and θ-Fe-carbides, χ-Fe_5C_2 was stable upon carburization at moderate temperatures and relatively low H_2/CO ratios. Wang et al. prepared a catalyst containing exclusively χ-Fe_5C_2 via carburization of a Raney® Fe precursor in a diluted synthesis gas feed [9]. The phase purity of the Fe catalyst led to a low CO_2 selectivity and high yield of C_2-C_{10} linear α-olefins.

Carburization of Fe in typical synthesis gas mixtures can lead to the deposition of less reactive carbon on the catalyst surface, especially during prolonged carburization at higher temperatures [10–13]. These carbon deposits lower the FT activity and further complicate fundamental studies of the relation between catalyst structure and performance. Gradual removal of these deposits can explain the often-observed induction period, during which the FT activity increases [4,10,14]. Carbon deposits may also build up during prolonged reaction, a significant cause of long-term deactivation, next to surface oxidation and active phase sintering [8,15,16]. These deposits may be removed by increasing the H_2 partial pressure or introducing H_2O in the feed [10,17]. A drawback of the latter approach is that H_2O can also lead to oxidation of the surface of the active Fe-carbide phase. A higher H_2 partial pressure, on the other hand, favors the formation of CH_4, which is considered a low-value by-product of the FT reaction. Traditional methods for removing carbon deposition include chemical regeneration via Soxhlet extraction [18], oxidative regeneration at medium temperatures (>100 °C) [19], and hydrogenation regeneration at high temperatures [20,21]. However, these approaches imply significant

* Corresponding authors.
E-mail addresses: peng.wang.hm@chnenergy.com.cn (P. Wang), e.j.m.hensen@tue.nl (E.J.M. Hensen).

https://doi.org/10.1016/j.jcat.2025.116030
Received 15 December 2024; Received in revised form 28 January 2025; Accepted 16 February 2025
Available online 27 February 2025

drawbacks, such as the partial destruction of the Fe-carbide structure or the sintering of particles, resulting in a loss of catalytic performance.

The goal of the research presented in this work was to develop a method for carbon removal that does not negatively affect the catalyst structure and performance. Since the simultaneous presence of different Fe phases troubles the fundamental study of the effect of carbon deposits, we started from a method that yields phase-pure χ-Fe_5C_2 as the main bulk phase [9]. Subsequently, different treatment methods consisting of passivation and reduction steps were applied to remove carbon deposits and decrease the induction period. The bulk structure of the as-prepared and treated χ-Fe_5C_2 catalysts was characterized by *in situ* XRD, *in situ* Mössbauer spectroscopy, and *in situ* X-ray absorption spectroscopy (XAS). Quasi-*in situ* XPS followed the transformation of Fe phases and the change of carbon species on the surface during treatment. Temperature-programmed hydrogenation and Raman spectroscopy were used to gain deeper insights into the nature and reactivity of carbon species after the different treatments. The results demonstrate the effectiveness of these treatments for removing carbonaceous deposits and provide insight into the role of carbonaceous species in the induction period and their potential application in the regeneration of deactivated Fe-based catalysts.

2. Experimental methods

2.1. Catalyst preparation

An amount of 5 g Fe-Al alloy powder (200 mesh, Hunan Xingyuan Powder Co., 50:50 by weight) was added into 30 ml of an 8 M KOH (Sigma-Aldrich) solution, under stirring and heating at 70 °C for 1.5 h to remove the Al of the alloy [9]. The resulting Fe solid was washed with demineralized water (12 times) and isopropanol (8 times) to remove K and Al from the slurry.

The obtained Fe powder was transferred into a sealed quartz tube in a glove box and dried in a flow of Ar gas at room temperature. Before carburization, the resulting Fe sample was passivated in a flow of 1.4 vol % O_2 in He at room temperature for 24 h to ensure safe operation. The resulting Raney® −like powder is labeled as R-Fe.

R-Fe was subsequently carburized in an H_2/CO/He gas mixture (90/5/18 ml/min) at atmospheric pressure. After heating to 350 °C for 6 h at a rate of 3 °C/min, the mixture was maintained at this temperature for 6 h. The carburized sample is labeled as χ-Fe_5C_2.

After carburization, three different treatment methods were applied. In the first method, the carburized sample was passivated in a 100 ml/min flow of 1.4 vol% O_2 in He at ambient pressure and room temperature for 8 h. This passivated sample is labeled as χ-Fe_5C_2-P. The second method was the same as the first one, with an additional reduction treatment in an H_2/He flow (90/18 ml/min) at ambient pressure and 250 °C for 0.5 h (heating rate 3 °C/min). The resulting sample, passivated and subsequently reduced, is labeled χ-Fe_5C_2-PR. The third method involved direct reduction in an H_2/He flow (90/18 ml/min) at ambient pressure and 250 °C for 0.5 h (heating rate 3 °C/min). This H_2-treated sample is labeled as χ-Fe_5C_2-R.

2.2. Catalyst characterization

The textural properties were determined by N_2 physisorption at −196 °C using a Micromeritics TriStar II 3020 instrument. Approximately 90 mg of sample was placed in a glass sample tube and subjected to overnight treatment at 150 °C in a N_2 flow. The Brunauer-Emmett-Teller (BET) method was employed to determine the catalyst's specific surface area.

Particle size was measured by TEM using a FEI Tecnai 20 Sphera transmission electron microscope operating at an acceleration voltage of 200 kV. The catalysts were dispersed in ethanol via ultrasonication and then deposited on a carbon-coated Cu grid.

Powder X-ray diffraction (XRD) patterns were obtained using a Bruker D2 Phaser powder diffractometer, which was equipped with a Cu Kα x-ray source and recorded with a scan speed of 0.02°/s in the 2θ range of 20–90°.

In situ XRD was carried out on a Rigaku D/max-2600/PC apparatus with a D/teX ultrahigh-speed detector and scintillation counter. The X-ray generator used a Cu rotating anode target with a maximum power of 9 kW. The *in situ* XRD patterns were recorded using an Anton Paar XRK-900 cell equipped with a CO/H_2/inert gas inlet system. All tests were conducted at a current of 40 mA and a voltage of 40 kV. The sample was carburized in the cell under H_2/CO/He gas (90/5/18 ml/min) at atmospheric pressure and 350 °C for 6 h using a 3 °C/min heating rate. The relative abundance and average crystallite size of different phases were determined using Rietveld refinement of the XRD patterns using GSAS-II (SVN version 5740).

Quasi-*in situ* X-ray photoelectron spectra (XPS) were acquired using a Kratos AXIS Ultra 600 spectrometer with a monochromatic Al Kα X-ray source ($h\nu = 1486.6$ eV). To prepare the sample for analysis, the samples were pressed into a pellet and placed on a stainless-steel stub, enabling the vacuum transfer of the sample from the reaction chamber into the XPS analysis chamber. A high-temperature reaction cell (Kratos, WX-530) was employed to pretreat the sample. The sample was carburized in an H_2/CO/He gas (90/5/18 ml/min) at atmospheric pressure and 350 °C for 6 h using a 3 °C/min heating rate. After carburization, the cell was cooled and evacuated, followed by the transfer of the sample to the XPS analysis chamber. Region scans were acquired at a pass energy of 40 eV with a step size of 0.1 eV, and survey scans were recorded at a pass energy of 160 eV with a step size of 0.5 eV. After the XPS measurement, the carburized sample was transferred *in vacuo* from the analysis chamber to the reaction cell and exposed to 100 ml/min 1.4 vol% O_2/He gas at ambient pressure for 8 h and reduced in H_2/He (90/18 ml/min) before the subsequent XPS measurement. The acquired XPS spectra were analyzed using Voigt functions after a Shirley background subtraction using CasaXPS software (version 2.3.23PR1.0).

Temperature-programmed hydrogenation (TPH) experiments were performed using a quartz tubular flow reactor equipped with an online mass spectrometer (Balzers TPG-300) and an online gas chromatograph (Compact GC 4.0). An amount of 50 mg fresh R-Fe was loaded in the reactor and subjected *in situ* to the carburization, passivation, and reduction treatments before the TPH experiment. The TPH was performed by heating the reactor to 800 °C at a 5 °C/min rate in a diluted H_2 flow (20 vol% H_2 in He, 50 ml/min). The effluent gas, which consisted primarily of CH_4 (>96 % of all hydrocarbons), was analyzed by a mass spectrometer.

Raman spectroscopy was carried out using a Witec Alpha 300 R Raman microscope with a CCD1 detector, a Zeiss 10x, NA = 0.25 objective, and a 300 g/mm grating. Spectra were acquired using a laser power of 2 mW at an excitation wavelength (λ_{exc}) of 532 nm, and data were collected over 60 s by averaging 20 scans.

In situ Mössbauer experiments were executed within an *in situ* high-pressure Mössbauer reaction cell developed at Reactor Institute Delft [22]. Transmission ^{57}Fe Mössbauer spectra were acquired at −153.15 °C with a sinusoidal velocity spectrometer using a ^{57}Co (Rh) source. Velocity calibration was conducted using an α-Fe foil at room temperature. The source and the absorbing samples were maintained at identical temperatures throughout the measurements. The Mössbauer spectra were fitted by using Mosswinn 4.0 software [23]. The carburization and post-treatments were performed *in situ* in the same way as described above, followed by cooling to −153.15 °C before Mössbauer spectra were acquired.

X-ray absorption spectroscopy (XAS) measurements at Fe K-edge (7112 eV for metallic Fe) were performed at the SAMBA beamline (SOLEIL synchrotron, France). *Ex situ* XAS spectra were collected in transmission mode using ionization chambers before and after the sample. *In situ* XAS spectra measurements were collected in fluorescence mode using a Ge-based fluorescence detector. The energy of the incident beam was calibrated by simultaneous measurement of a Fe foil at room

temperature. For *ex situ* XAS measurements, the samples were pressed into self-supporting pellets and sealed in Kapton tape. These measurements were done at room temperature. *In situ* XAS was performed using a quartz capillary reactor in which the sieved sample (125–250 um) was held between two quartz wool plugs. The capillary reactor was placed horizontally on the stage and heated by a gas blower. The temperature inside the capillary reactor was calibrated using a K-type thermocouple. The catalyst was carburized at ambient pressure in an H_2/CO flow of 19 ml/min gas (H_2/CO ratio = 18) at 350 °C for 4 h using a 3 °C/min heating rate. After carburization, the reactor was cooled to room temperature and passivated in a 1.4 vol% O_2/He flow of 10 ml/min for 6 h. Then, the sample was reduced in a flow of 16 ml/min H_2/He (H_2/He ratio = 5) at 250 °C for 0.5 h. The reaction was performed in 27 ml/min syngas (H_2/CO ratio = 2) at 250 °C and 5 bar. All spectra were energy calibrated, pre-edge subtracted, and post-edge normalized using the Fastosh software package developed at the SAMBA beamline. Multi-curve regression-alternate least square (MCR-ALS) analysis was also done with Fastosh.

2.3. Catalytic activity measurements

An amount of 20 mg R-Fe mixed with 3 ml SiC was loaded in a stainless-steel tubular flow reactor placed in a Microactivity Reference reactor unit. The reactor dimensions were 9 mm (internal diameter) × 305 mm (length) with an internal volume of 20 ml. The reactor was operated in down-flow mode. Thermal mass flow controllers provided the reactor feed. The R-Fe catalyst precursor was carburized in the reactor in an H_2/CO/He gas mixture (90/5/18 ml/min) at 350 °C for 6 h using a 3 °C/min heating rate and at ambient pressure. Subsequent passivation and reduction treatments were also performed *in situ*. The catalytic performance was evaluated at a pressure of 20 bar and a temperature of 250 °C using an H_2/CO/He/Ar mixture (4/2/19/0.2 ml/min). The gas hourly space velocity (GHSV) was 150 $L{\cdot}g^{-1}{\cdot}h^{-1}$. Mass and heat transfer limitations were confirmed to be absent (see Supporting Information). The reactor effluent was analyzed using an online gas chromatograph (Thermo Fisher Scientific Trace 1300) equipped with XL-Sulfur and Molsieve 5A columns (TCD) and Rtx-1 column (FID).

Quantitative analysis involved the use of the relative response factor $f_{i,Ar}$ of compound i relative to the Ar internal standard as determined by Equation (1). The unknown volumetric flow rate of compound i in the outlet was then obtained using Equation (2).

$$f_{i,Ar} = \frac{A_{i,in}/F_{i,in}}{A_{Ar,in}/F_{Ar,in}} = \frac{A_{i,out}/F_{i,out}}{A_{Ar,out}/F_{Ar,out}} \quad (1)$$

$$F_{i,out} = \frac{A_{i,out}F_{Ar,out}}{A_{Ar,out}f_{i,Ar}} \quad (2)$$

where the integrated areas $A_{i,in}$ and $A_{i,out}$ correspond to the peak of compound i in the inlet and outlet, and $F_{i,in}$ and $F_{i,out}$ represents the volumetric flow rate in the inlet and outlet.

The CO conversion (X_{CO}) and the product selectivity (S_j) are calculated using the following equations. The unknown value of $F_{i,out}$ is substituted by Equation (2).

$$X_{CO} = 1 - \frac{F_{CO,out}/F_{Ar,out}}{F_{CO,in}/F_{Ar,in}} \quad (3)$$

$$S_j = \frac{F_{Ar,in}F_{j,out}}{F_{Ar,out}F_{CO,in}X_{CO}} \quad (4)$$

where $F_{j,out}$ represents the volumetric flow rate of products j ($j \in i$, representing all compounds except the reactant CO). We carried out a catalytic test three times to determine the experimental accuracy of the catalytic activity measurements. The standard deviation of the CO conversion was ~ 0.4 %.

Deactivation and regeneration tests were performed using 150 mg of the R-Fe sample mixed with SiC. The precursor was subjected to *in situ* carburization to 350 °C for 6 h at a 3 °C/min heating rate in an H_2/CO/He gas mixture (90/5/18 ml/min). The reaction was conducted at a temperature of 290 °C, a pressure of 1.5 bar and a space velocity of 20 $L{\cdot}g^{-1}{\cdot}h^{-1}$ (H_2/CO = 10). After deactivation, the reactor was cooled to room temperature in Ar gas. Regeneration involved passivation followed by reduction, using the same procedure described above. This deactivation-regeneration process was repeated for two cycles. The MS signal of CH_4 ($m/z = 15$) was continuously monitored by an online mass spectrometer (ESS CatalySys).

3. Results and discussion

3.1. Carburization and treatment of χ-Fe_5C_2

Carburization

In situ XRD was used to follow the carburization of R-Fe (Fig. S1). The main phases identified in these experiments are shown in Table 1. The patterns of the fresh sample and those recorded in the carburization mixture at low temperatures contain diffraction lines of α-Fe, the main phase in R-Fe. Weak (220) and (511) diffraction lines of Fe_3O_4 can also be observed. During carburization, the intensities of the α-Fe and Fe_3O_4 lines decrease, starting from 250 °C. These diffraction lines of the precursor nearly completely disappear at 300 °C. Simultaneously, diffraction lines assignable to χ-Fe_5C_2 (*PDF# 89-8968*) appear, due to the formation of the χ-Fe_5C_2. At 300 °C, the combined fraction of α-Fe and Fe_3O_4 has decreased to 28 wt% of the total Fe. At 350 °C, α-Fe and Fe_3O_4 lines have entirely vanished, showing that pure χ-Fe_5C_2 has been formed. Scherrer analysis was used to estimate the crystallite sizes of the different phases (Table 1). The average crystallite size of α-Fe decreases from 30 nm at 150 °C to 15 nm at 300 °C. The Fe_3O_4 crystallite size grows from 9 nm to 14 nm, followed by a slight decrease to 12 nm at 300 °C. The crystallite size of χ-Fe_5C_2, which is 24 nm at 300 °C, only increases slightly to 27 nm after 6 h carburization at 350 °C.

Passivation and reduction treatments

We then used *ex situ* XRD to characterize the samples obtained after the passivation and reduction treatments. Fig. 1 shows that the *ex situ* XRD patterns are comparable to the data obtained by *in situ* XRD (Fig. S1). These results show that all treatments retain χ-Fe_5C_2 as the main crystal phase. TEM images (Fig. S2) show that the average particle size of the fresh R-Fe sample is 28 ± 6 nm and does not significantly change during carburization and further treatments. The specific surface areas of these samples provided in Table S1 show a significant increase

Table 1
Rietveld refinement of *in situ* XRD patterns of R-Fe during stepwise carburization (different temperatures and dwell times at 350 °C).

Carburization condition	Phase	Content (wt.%)	d (nm)	R_{wp} (%)
150 °C	α-Fe	86	30	1.74
	Fe_3O_4	13	9	
	χ-Fe_5C_2	0	0	
200 °C	α-Fe	66	29	1.12
	Fe_3O_4	34	11	
	χ-Fe_5C_2	0	0	
250 °C	α-Fe	62	28	1.57
	Fe_3O_4	38	14	
	χ-Fe_5C_2	0	0	
300 °C	α-Fe	14	15	1.34
	Fe_3O_4	14	12	
	χ-Fe_5C_2	72	24	
350 °C, 0 h	α-Fe	0	0	1.48
	Fe_3O_4	0	0	
	χ-Fe_5C_2	100	25	
350 °C, 6 h	α-Fe	0	0	1.47
	Fe_3O_4	0	0	
	χ-Fe_5C_2	100	27	

The metrics are mass weight percent (wt.%), average crystallite size (d), and the weighted profile R-factor determined during Rietveld refinement (R_{wp}).

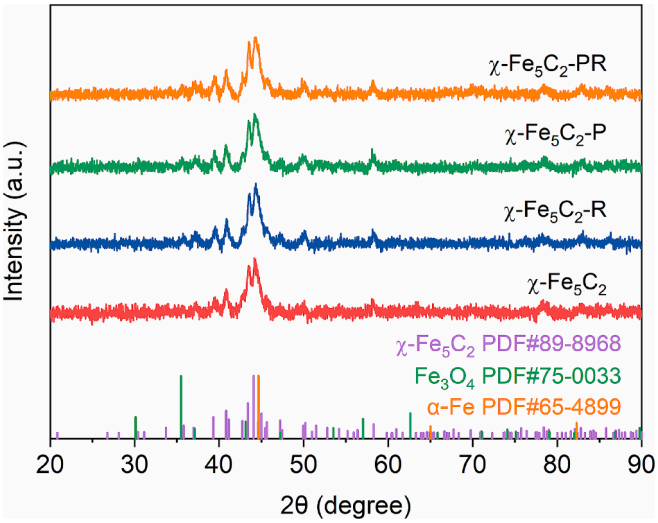

Fig. 1. *Ex situ* XRD patterns of the as-prepared and treated χ-Fe_5C_2 samples.

in the surface area after carburization. We tentatively attribute this to a layer of porous carbonaceous deposits. The formation of such a layer of carbon is also observed by TEM.

3.2. Catalytic activity measurements

The catalytic performance of as-prepared and treated χ-Fe_5C_2 catalysts is presented in Fig. 2. The CO conversion of as-prepared χ-Fe_5C_2 exhibits a prolonged induction period (> 25 h), with CO conversion increasing from 1.5 % at the start of the reaction to 10.6 % after 60 h. The χ-Fe_5C_2 catalysts treated solely by reduction or passivation, i.e., χ-Fe_5C_2-R or χ-Fe_5C_2-P, respectively, exhibit a very similar induction period, suggesting that these treatments did not significantly affect the as-prepared sample. However, when as-prepared χ-Fe_5C_2 was first passivated in O_2, followed by a reduction in H_2 (χ-Fe_5C_2-PR), the initial CO conversion is substantially higher at ca. 8 %, and the induction period is shorter. The induction period can be caused by phenomena such as the transformation of Fe phases from Fe-oxide or less active Fe-carbide phases to more active Fe-carbide phases [4,14] or the removal of

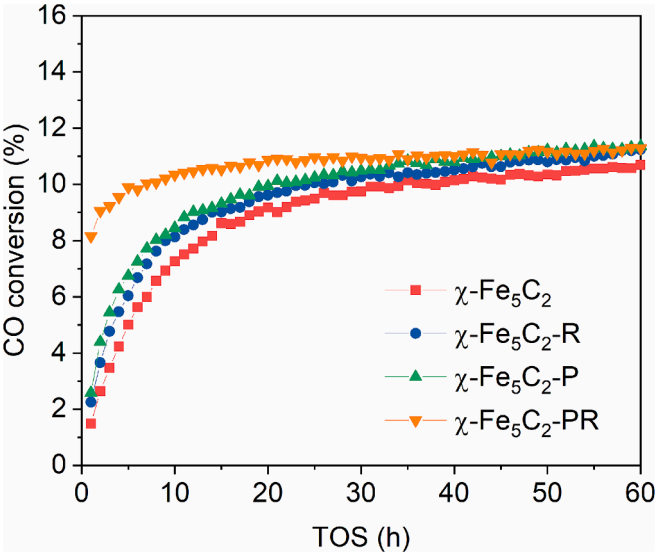

Fig. 2. CO conversion of *in situ* carburized (χ-Fe_5C_2) and treated χ-Fe_5C_2 samples as a function of the time on stream (conditions: 250 °C, 20 bar, 150 $L{\cdot}g^{-1}{\cdot}h^{-1}$, $H_2/CO = 2$).

inactive carbonaceous deposits that obstruct the active sites [4,10]. We next studied the way that the passivation-reduction treatment affected the induction period.

Fig. 3 presents the product distribution of the FT reaction. After the induction period, all catalysts exhibit a comparable CO_2 selectivity of ~ 4 %, which is low compared to other Fe-based catalysts [7,24–26]. The selectivities to CH_4, C_2-C_4, and C_{5+} hydrocarbons are 16, 32, and 49 %, respectively. The nearly unchanged product distribution of the as-prepared and differently treated samples after the prolonged induction period indicates that the nature of the active sites did not change by the reduction and oxidative treatments. Thus, it is reasonable to state that the passivation-reduction treatment (χ-Fe_5C_2-PR) does not influence the catalytic behavior of the active sites. Nevertheless, it significantly shortens the induction period of the as-prepared catalyst, during which both the activity and the selectivity to CH_4 and CO_2 change. The other samples initially show lower CO_2 and higher CH_4 selectivity than the χ-Fe_5C_2-PR sample. To verify that the passivation-reduction treatment removes carbonaceous deposits from the surface without affecting the catalyst structure, the bulk structure of the as-prepared and treated catalysts was studied by *in situ* Mössbauer spectroscopy and *in situ* XANES. Quasi-*in situ* XPS was applied to examine the surface composition.

3.3. Characterization of bulk and surface phases

^{57}Fe Mössbauer spectra of *in situ* carburized R-Fe not only confirm the formation of χ-Fe_5C_2, but also show that the different post-treatment methods do not affect the bulk structure (Table 2). The superposition of three sextuplets observed in the Mössbauer spectra (Fig. S3) corresponds to the occupation of three different interstitial sites in the Fe lattice [27,28], indicating the co-existence of χ-Fe_5C_2 (I), χ-Fe_5C_2 (II), and χ-Fe_5C_2 (III) species. The relative spectral areas of the three sites are not equal to the theoretical ratio of Fe (I): Fe (II): Fe (III) = 2:2:1, which was derived from the populations of the individual crystallographic locations in the χ-Fe_5C_2 bulk lattice. The non-stoichiometry of the Fe-carbide or a small amount of another Fe-carbide can cause the difference [29]. Possibly, the sextuplet of a small amount of θ-Fe_3C overlaps with the Fe (I) sextuplet of χ-Fe_5C_2. Nevertheless, it can be seen from Table 2 that the changes in carbide composition after the different treatment procedures remain within the experimental uncertainty of 3 %. Thus, Mössbauer analysis confirms the XRD results (Fig. 1) that the χ-Fe_5C_2 phase is unchanged upon the different post-treatment procedures.

The results of *in situ* X-ray absorption near-edge structure (XANES) at Fe K-edge during the carburization, passivation, reduction treatments and reaction are shown in Fig. 4. The typical absorption edges and pre-edge features of the 1s to 3d transitions at 7114 eV can be observed [30,31]. Fig. 4a shows the changes in the XANES spectra during carburization. The absorption edge energy shifts to higher energies during the first 1.5 h, corresponding to the oxidation of Fe species during the heating stage of the carburization (Fig. 4b). In the final 4.5 h of the carburization, the absorption edge energy shifts again to lower values, as highlighted in Fig. 4c. Compared with the XANES reference spectra, the XANES spectrum of the final state after carburization resembles that of the χ-Fe_5C_2. This supports the XRD and Mössbauer spectroscopy findings that χ-Fe_5C_2 is the dominant phase. The brief initial oxidation was also observed by *in situ* XRD (Fig. S1). Moreover, MCR-ALS analysis based on reference compounds (Fig. 4d) exemplifies the conversion of metallic Fe into χ-Fe_5C_2 during carburization. In agreement with the *in situ* XRD analyses (Fig. S1 and Table 1), an amount of $Fe(O)_x$ (x = 0–1.33) forms at the initial stage of carburization at low temperatures, which is converted to pure χ-Fe_5C_2 upon prolonging the carburization treatment. *In situ* XANES spectra of subsequent treatments (Fig. 4e-g) are nearly unchanged. This implies that the χ-Fe_5C_2 phase is unaltered during the passivation and reduction treatments and the reaction, consistent with the *in situ* Mössbauer spectroscopy results (Tables 2 and S2). The finding that the passivation-reduction treatment did not affect the activity and

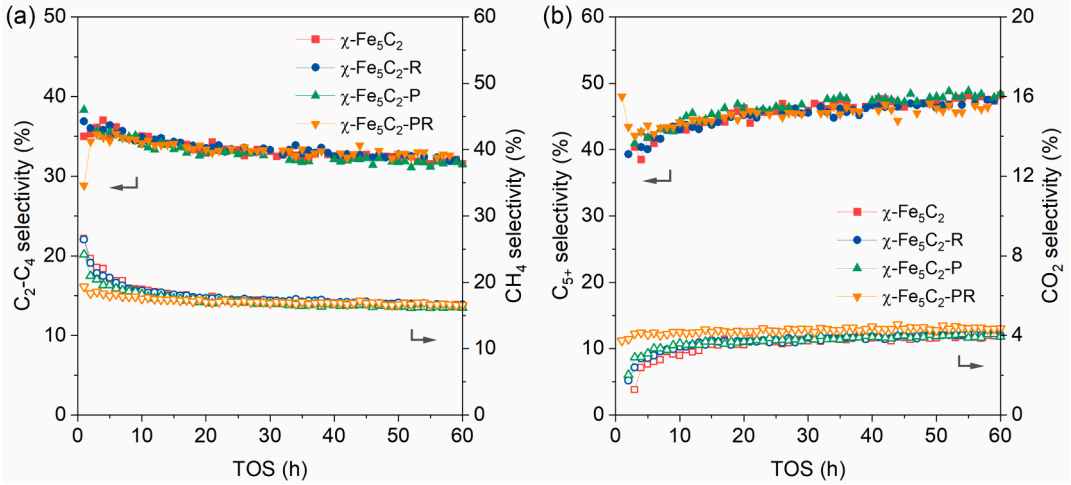

Fig. 3. Product distribution during FT reaction of *in situ* carburized (χ-Fe_5C_2) and treated χ-Fe_5C_2 samples as a function of the time on stream (conditions: 250 °C, 20 bar, 150 $L{\cdot}g^{-1}{\cdot}h^{-1}$, $H_2/CO = 2$).

Table 2
Fitting parameters of *in situ* ^{57}Fe Mössbauer spectra of χ-Fe_5C_2 catalysts after different treatments.

Samples	IS ($mm{\cdot}s^{-1}$)	QS ($mm{\cdot}s^{-1}$)	Hyperfine field (T)	Γ ($mm{\cdot}s^{-1}$)	Phase	Spectral contribution (%)
χ-Fe_5C_2	0.25	–	24.2	0.44	χ-Fe_5C_2 (I) / θ-Fe_3C	44
	0.18	–	21.0	0.46	χ-Fe_5C_2 (II)	37
	0.15	–	13.1	0.45	χ-Fe_5C_2 (III)	19
χ-Fe_5C_2-R	0.25	–	24.2	0.46	χ-Fe_5C_2 (I) / θ-Fe_3C	46
	0.18	–	21.1	0.49	χ-Fe_5C_2 (II)	36
	0.16	–	13.3	0.45	χ-Fe_5C_2 (III)	18
χ-Fe_5C_2-P	0.26	–	24.4	0.43	χ-Fe_5C_2 (I) / θ-Fe_3C	43
	0.19	–	21.1	0.48	χ-Fe_5C_2 (II)	38
	0.16	–	13.4	0.42	χ-Fe_5C_2 (III)	19
χ-Fe_5C_2-PR	0.25	–	24.3	0.43	χ-Fe_5C_2 (I) / θ-Fe_3C	43
	0.18	–	21.1	0.47	χ-Fe_5C_2 (II)	38
	0.16	–	13.3	0.42	χ-Fe_5C_2 (III)	19

Experimental uncertainties: Isomer shift: I.S. ± 0.02 mm s^{-1}; Quadrupole splitting: Q.S. ± 0.02 mm s^{-1}; Line width: Γ ± 0.03 mm s^{-1}; Hyperfine field: ± 0.1 T; Spectral contribution: ± 3 %.

product distribution at the steady state shows that its effectiveness in shortening the induction period. Other methods proposed in the literature substantially affect catalyst structure and performance [20,21].

As Mössbauer spectroscopy, XRD, and XAS yield limited information about the catalytic surface sites, quasi-*in situ* XPS was used to elucidate possible differences at the surface. Fe 2p and C 1s XPS spectra are shown in Fig. 5. After carburization, the Fe 2p spectrum exhibits a prominent peak at ~ 706.90 eV, typical for zero-valent Fe in Fe-carbide [5,32]. Peaks due to oxidized Fe^{2+} and Fe^{3+} species are visible at higher binding energies [3,32,33]. This indicates that carburization leads to almost complete reduction of Fe. The slight oxidation of Fe may be caused by the deposition of oxygen-containing species derived from CO during carburization [5]. The C 1s spectra show that carburization leads to the formation of C species associated with metallic carbide (FeC_x) and carbonaceous surface deposits, primarily composed of sp^2 graphitic carbon (C=C), and some sp^3 C linked to saturated hydrocarbons (C–C) [34–36]. Some oxidized carbon species can also be observed after carburization. The composition of the carbonaceous surface deposits, as calculated through deconvolution, is presented in Table 3. This table also lists the $C{=}C/FeC_x$ ratio, representing the amount of graphitic carbon relative to the amount of carbide carbon, which can be used as a relative measure for the coverage of the carbide surface by graphitic deposits. The reduction-only treatment (χ-Fe_5C_2-R) does not noticeably change the amount of oxidized Fe and carbon species compared to the as-prepared carburized catalyst χ-Fe_5C_2. However, the passivation-only treatment (χ-Fe_5C_2-P) leads to a higher content of oxidized Fe on the surface, while Mössbauer and XANES spectra demonstrate that the bulk carbide phase is not significantly impacted. Shroff et al. reported that careful passivation does not lead to magnetite due to the protection of the underlying carbide by the carbon overlayer [37,38]. Our C 1s spectra also show more oxidized carbon species, as follows from the appearance of peaks assignable to oxygenated carbon species (C-O-C, C=O, O-C=O) [39,40]. The noticeable increase in the ratio of $C{=}C/FeC_x$ is due to a higher degree of oxidation of the Fe surface, resulting in less FeC_x compared to graphitic carbon. After subsequent reduction, the original low oxidation degree of Fe is restored, and the oxygenated carbon formed during passivation disappears. The Fe speciation of the parent Fe-carbide surface undergoes very slight changes upon a reduction or passivation-reduction treatment. As the Fe reduction degrees of the χ-Fe_5C_2-R and χ-Fe_5C_2-PR samples are comparable, the shorter induction period observed with the χ-Fe_5C_2-PR catalyst cannot be attributed to Fe speciation. Table 3 and S3 show that concurrently, the amount of graphitic carbon in χ-Fe_5C_2-PR is drastically reduced compared to χ-Fe_5C_2. The passivation treatment alters the oxidation state of surface Fe and carbonaceous deposits such that the amount of graphitic carbon is reduced substantially after subsequent reduction. To understand the changes in carbonaceous deposits in more detail, TPH analysis and Raman spectroscopy were performed.

TPH was employed to quantify and identify the carbon species in the catalysts. Notably, during TPH, carbon deposits lead to the formation of CH_4 (Fig. 6a) and CO_2 (Fig. 6b). The peaks are assigned to various carbon species. The α-carbon feature in Fig. 6a can be attributed to the

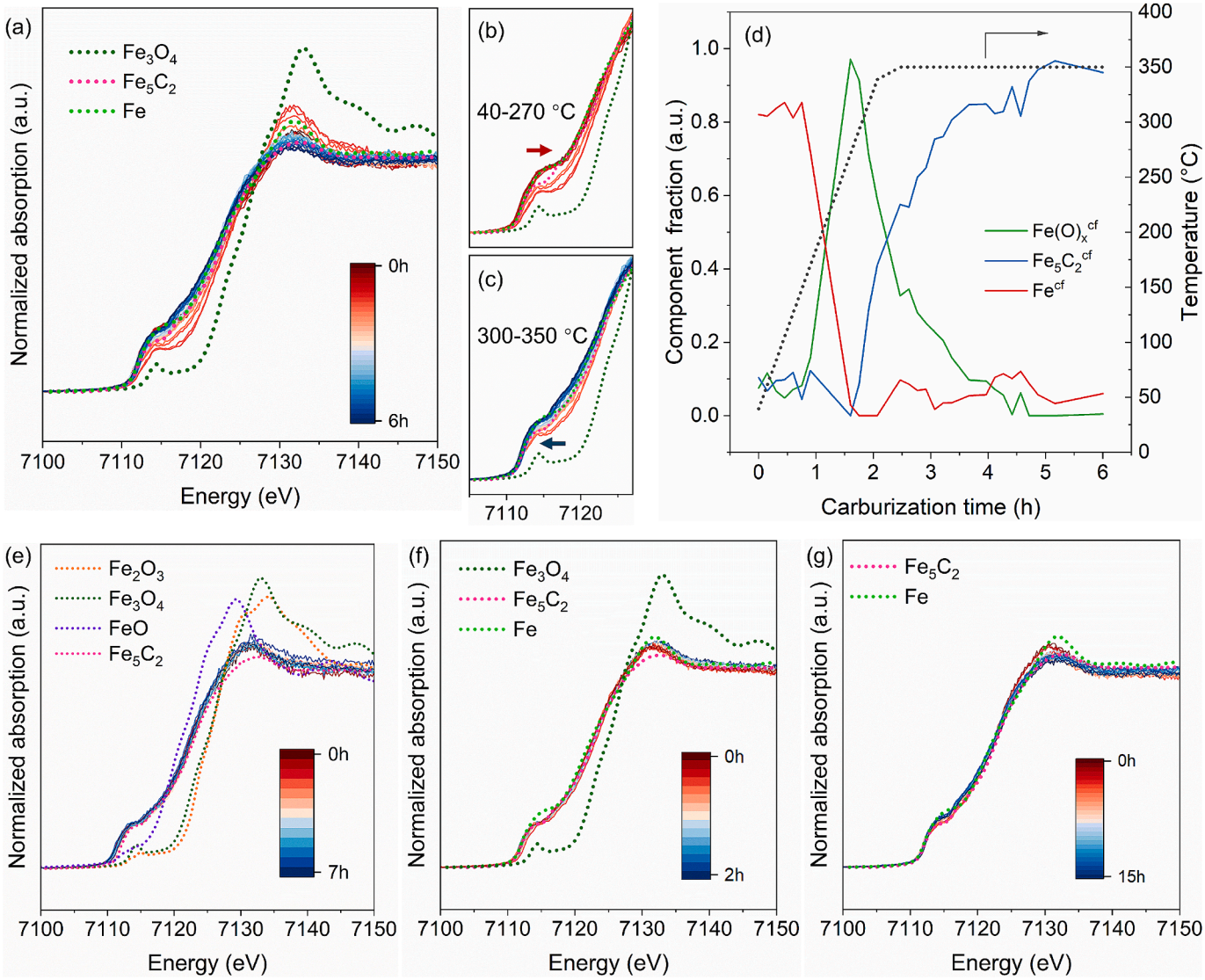

Fig. 4. *In situ* XANES measurements of the samples following (a) carburization of R-Fe, (e) passivation of as-prepared χ-Fe_5C_2, (f) reduction of passivated χ-Fe_5C_2, and (g) reaction over passivated-reduced χ-Fe_5C_2. (b) and (c) are the enlargements of (a): (b) shows the first 1.5 h of the carburization and (c) the last 4.5 h. (d) The fractions of spectral components during the carburization period, as determined by MCR-ALS. The superscript "cf" refers to components derived by curve fitting (detailed fitting results in Fig. S5).

hydrogenation of reactive surface carbon species like atomic carbon, surface carbide, or disordered polymeric carbon. The β-carbon feature, represented by a peak at intermediate temperatures (450–510 °C), can be attributed to polymeric aggregates of carbon. The γ-carbon feature, which occurs at high temperatures (510–600 °C), can be attributed to the hydrogenation of bulk Fe-carbide. The signal above 600 °C is due to low-reactive graphitic carbon, which has been reported to delay the reduction of bulk carbide [11,17,41]. The TPH profile of χ-Fe_5C_2-PR shows a slightly different shape than χ-Fe_5C_2. The peak corresponding to high-temperature γ-carbon is shifted to lower temperatures, which suggests that the passivation-reduction treatment changed the structure of graphitic carbon. Simultaneously, a slight increase in highly reactive α-carbon at the expense of β-carbon is observed. α-Carbon can be hydrogenated easily during the initial stage of the reaction, thereby facilitating the exposure of active surface sites. Xu et al. proposed that the initial catalytic activity is positively correlated with the amount of reactive α-carbon at the surface [41]. The CO_2 TPH profiles in Fig. 6b display two peaks, which are much more intense for χ-Fe_5C_2-P than for the other samples. The low-temperature peak originates from weakly adsorbed oxidized carbon species on the catalyst surface. In contrast, the high-temperature CO_2 peak indicates the presence of strongly adsorbed oxidized carbon species on the catalyst surface [42–44]. The more intense CO_2 TPH peaks for χ-Fe_5C_2-P show that the oxidative passivation treatment leads to more oxidized carbon species, in agreement with the C 1 s XPS results. Notably, when the passivated sample is reduced (χ-Fe_5C_2-PR), the CO_2 peaks nearly vanish, being lower in intensity than for χ-Fe_5C_2 and χ-Fe_5C_2-R, also in agreement with the XPS results.

The transformation of carbon species was also investigated by Raman spectroscopy (Fig. 7). After carburization, bands with Raman shifts of 1350 cm^{-1} and 1610 cm^{-1} can be attributed to the D- and G-bands of carbon [45–47]. The spectra were fitted by Lorentzian/Gaussian bands labeled D_1, D_3, D_4, and G [48–50]. The G band represents carbon species with an ordered graphitic structure, whereas the D bands relate to graphitic carbon species with defects and amorphous, disordered carbon. The D_1 band is attributed to a disordered graphite lattice with A_{1g} symmetry commonly found at the edges of graphene layers. Oxidized carbon species can also contribute to the D_1 band [50]. The D_2 band is due to disordered graphite with E_{2g} symmetry, typically occurring in graphene layers. The D_3 band has been commonly associated with amorphous carbon. The D_4 band points to a disordered

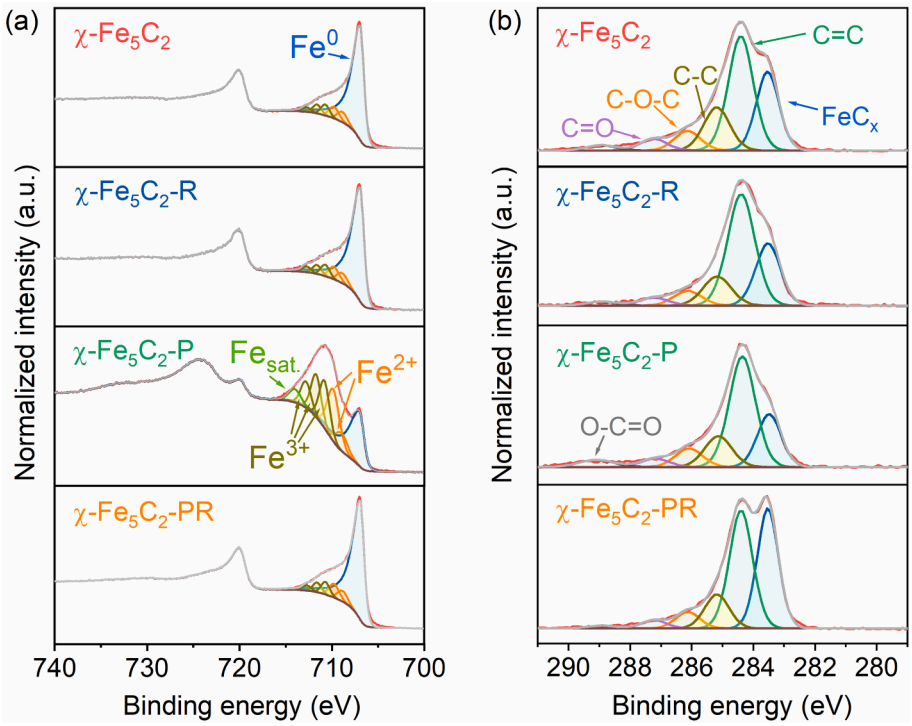

Fig. 5. Quasi-*in situ* XPS spectra of (a) Fe 2p and (b) C 1 s regions of the as-prepared sample (χ-Fe_5C_2), χ-Fe_5C_2 after reduction (χ-Fe_5C_2-R), χ-Fe_5C_2 after passivation (χ-Fe_5C_2-P), and χ-Fe_5C_2 after passivation-reduction (χ-Fe_5C_2-PR).

Table 3
Surface speciation based on deconvolution of Fe 2p and C 1s XPS spectra shown in Fig. 5.

Sample	$Fe^0/(Fe^0 + Fe^{2+,3+})$, %	C=C/FeC_x, peak ratio	Oxygenated Carbon[a]/total carbon, %
χ-Fe_5C_2	79.6	1.6	14.8
χ-Fe_5C_2-R	78.8	1.7	12.8
χ-Fe_5C_2-P	30.6	2.3	17.1
χ-Fe_5C_2-PR	78.5	1.1	10.3

[a] : total of all oxygenated carbon species (C-O-C, C=O, O-C=O).

graphitic lattice with A_{1g} symmetry, such as in polyenes [48].

Fig. 7 shows the impact of different treatments on the carbonaceous deposits. A higher $I(D_1)/I(G)$ ratio indicates more disordered and amorphous carbonaceous deposits. The $I(D_1)/I(G)$ ratios after reduction or passivation increase slightly, showing the minor effect of these treatments on the carbonaceous deposits. Table S4 lists the intensities of the G and D bands. The passivated sample exhibits a slightly higher amount of carbon species in the D_1 band together with a decrease in the G band, indicating the formation of oxidized carbon species during passivation [50]. Hence, the slightly increased $I(D_1)/I(G)$ ratio observed upon passivation may be caused by more oxidized carbon species, consistent with the quasi-*in situ* XPS results in Table 3. Additionally, Janbroers et al. used TEM-EELS to show that the oxidation of Fe-carbide was accompanied by the obvious build-up of amorphous carbon [38]. $I(D_3)$ attributed to the amorphous carbon in χ-Fe_5C_2-P shows only a slight increase, suggesting the passivation of the surface is mild. Notably, as presented in Table S4, the passivation-reduction treatment shows a more significant increase in the $I(D_1)/I(G)$ ratio, which indicates a

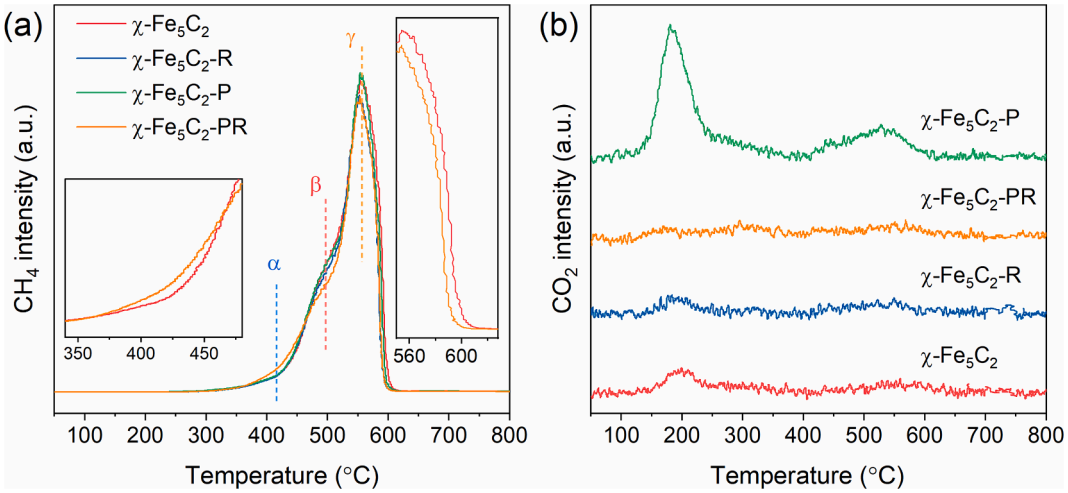

Fig. 6. TPH profiles of the treated samples: MS signals of (a) CH_4 ($m/z = 15$) and (b) CO_2 ($m/z = 44$).

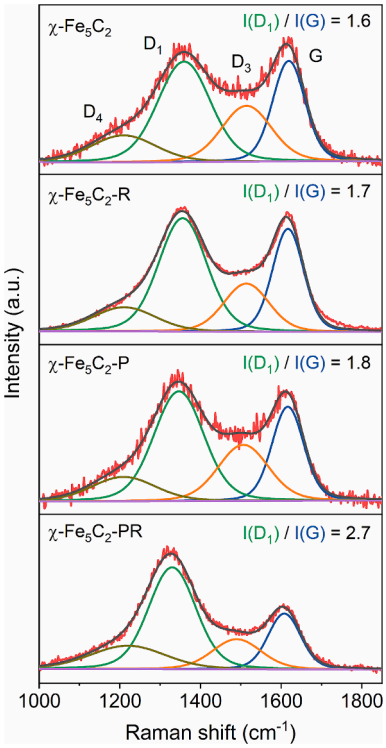

Fig. 7. Raman spectra of treated samples after carburization (χ-Fe_5C_2), reduction (χ-Fe_5C_2-R), passivation (χ-Fe_5C_2-P) and passivation-reduction (χ-Fe_5C_2-PR).

pronounced shift toward more disordered and amorphous carbon deposits. This treatment decreases the amount of ordered graphitic carbon from 25 % in χ-Fe_5C_2 to 18 % in χ-Fe_5C_2-PR and increases the amount of carbon in the D_1 and D_4 bands. This demonstrates that the passivation-reduction process transforms the ordered graphite into disordered graphite with edges or polyenes, making the carbon structure more reactive. This disordered structure is easier to remove under reaction conditions, making the induction period for χ-Fe_5C_2-PR shorter than for χ-Fe_5C_2 (Fig. 2).

Aside from causing the long induction period, carbon deposition also leads to the deactivation of Fe-based catalysts during reaction, especially at low pressures [17,51]. Chai et al. found the buildup of carbon deposits on Fe-carbide, accompanied by its deactivation, occurred due to the slow hydrogenation of carbon species at atmospheric pressure [17]. To investigate the potential of passivation-reduction treatment for regenerating Fe catalysts deactivated by carbon deposition, the χ-Fe_5C_2 catalyst was deactivated by CO hydrogenation at atmospheric pressure, followed by a regeneration procedure based on the passivation-reduction treatment. As shown in Fig. S7, in each reaction cycle, the amount of CH_4 decreases with time on stream, indicating deactivation. However, after each passivation-reduction cycle, the activity of the χ-Fe_5C_2 catalyst is restored, demonstrating the effectiveness of the regeneration process and further confirming the carbon removal effect of the passivation-reduction treatment. Unlike traditional regeneration methods [18–20], the presented mild carbon removal procedure can remove carbon deposits without affecting the active phase and catalytic activity. Another benefit is that the passivation-reduction procedure does not require very different conditions from the ongoing FT reaction, facilitating integration in practical FT reactors.

4. Conclusion

Phase-pure χ-Fe_5C_2 was successfully prepared by carburization of metallic R-Fe but appears to be covered by carbonaceous deposits. These deposits hamper fundamental catalytic studies. Several treatment methods have been tested to remove these carbon deposits. We comprehensively studied the influence of various treatments on the catalytic performance and the structure of Fe species and carbonaceous deposits of the χ-Fe_5C_2 catalyst. It was revealed that individual passivation or reduction treatments exert a minor effect on the carbonaceous deposits of the χ-Fe_5C_2 catalyst and the induction period. In contrast, a combined passivation-reduction treatment leads to a significant transformation of these carbonaceous deposits. The passivation-reduction treatment process significantly enhances the initial activity. Detailed characterization techniques show that during the passivation step, the carbonaceous deposits are transformed from an ordered graphitic structure to a disordered and oxidized carbon structure, which can be removed easily by subsequent reduction. The carbonaceous deposits must be activated before a reduction treatment can remove them. The catalyst structure and performance remain unaltered during these treatments in contrast to methods described earlier. Additionally, this newly developed method for removing carbonaceous deposits opens possibilities for regenerating catalysts deactivated by deposited carbon. This finding highlights the potential of enhancing catalyst performance through strategic treatment methods that target altering carbonaceous deposit structures, especially addressing induction period or deactivation issues caused by deposited carbon.

CRediT authorship contribution statement

Shiyue Li: Writing – original draft, Investigation, Formal analysis, Conceptualization. **Robert Pestman:** Writing – review & editing, Supervision, Conceptualization. **A. Iulian Dugulan:** Methodology, Formal analysis. **Zhuowu Men:** Supervision. **Peng Wang:** Writing – review & editing, Investigation, Conceptualization. **Emiel J.M. Hensen:** Investigation.

Declaration of competing interest

The authors declare that they have no known competing financial interests or personal relationships that could have appeared to influence the work reported in this paper.

Acknowledgments

Shiyue Li acknowledges the financial support from the China Scholarship Council. This work was supported by the National Key Research and Development Program of China (No. 2022YFB4101400) and CHN Energy Science and Technology innovation project (No. GJPT-23-18). We acknowledge Dr. Emiliano Fonda, Guillaume Alizon, Dr. Hao Zhang, Dr. Liang Liu, and Yonghui Fan for the assistance in using and operating the SAMBA beamline at SOLEIL Synchrotron under proposal No. 20220306.

Appendix A. Supplementary material

Supplementary data to this article can be found online at https://doi.org/10.1016/j.jcat.2025.116030.

Data availability

Data will be made available on request.

References

[1] K.T. Rommens, M. Saeys, Molecular views on Fischer–Tropsch synthesis, Chem. Rev. 123 (2023) 5798–5858, https://doi.org/10.1021/acs.chemrev.2c00508.
[2] M. Martinelli, M.K. Gnanamani, S. Leviness, G. Jacobs, W.D. Shafer, An overview of Fischer–Tropsch synthesis: XtL processes, catalysts and reactors, Appl. Catal. A 608 (2020) 117740, https://doi.org/10.1016/j.apcata.2020.117740.

[3] C. Yang, H. Zhao, Y. Hou, D. Ma, Fe_5C_2 nanoparticles: a facile bromide-induced synthesis and as an active phase for Fischer–Tropsch synthesis, J. Am. Chem. Soc. 134 (2012) 15814–15821, https://doi.org/10.1021/ja305048p.

[4] Q. Chang, C.H. Zhang, C.W. Liu, Y.X. Wei, A.V. Cheruvathur, A.I. Dugulan, J. W. Niemantsverdriet, X.W. Liu, Y.R. He, M. Qing, L.R. Zheng, Y.F. Yun, Y. Yang, Y. W. Li, Relationship between iron carbide phases (ε-Fe_2C, Fe_7C_3, and χ-Fe_5C_2) and catalytic performances of Fe/SiO_2 Fischer–Tropsch catalysts, ACS Catal. 8 (2018) 3304–3316, https://doi.org/10.1021/acscatal.7b04085.

[5] L. Niu, X. Liu, X. Zhou, C. Huo, J. Xu, X. Wen, J.W. Niemantsverdriet, Y. Yang, Y. Li, Genesis of an Fe_5C_2@Fe_3O_4 Core/shell structure during CO carburization of metallic iron nanoparticles, J. Catal. 407 (2022) 97–103, https://doi.org/10.1016/j.jcat.2022.01.029.

[6] Y. Yang, H. Xiang, L. Tian, H. Wang, C. Zhang, Z. Tao, Y. Xu, B. Zhong, Y. Li, Structure and Fischer–Tropsch performance of iron-manganese catalyst incorporated with SiO_2, Appl. Catal. A 284 (2005) 105–122, https://doi.org/10.1016/j.apcata.2005.01.025.

[7] T. Herranz, S. Rojas, F. Perezalonso, M. Ojeda, P. Terreros, J. Fierro, Genesis of iron carbides and their role in the synthesis of hydrocarbons from synthesis gas, J. Catal. 243 (2006) 199–211, https://doi.org/10.1016/j.jcat.2006.07.012.

[8] E. de Smit, F. Cinquini, A.M. Beale, O.V. Safonova, W. van Beek, P. Sautet, B. M. Weckhuysen, Stability and reactivity of Epsilon-Chi-theta iron carbide catalyst phases in Fischer–Tropsch synthesis: controlling μ_C, J. Am. Chem. Soc. 132 (2010) 14928–14941, https://doi.org/10.1021/ja105853q.

[9] P. Wang, F.K. Chiang, J. Chai, A.I. Dugulan, J. Dong, W. Chen, R.J.P. Broos, B. Feng, Y. Song, Y. Lv, Q. Lin, R. Wang, I.A.W. Filot, Z. Men, E.J.M. Hensen, Efficient conversion of syngas to linear α-olefins by phase-pure χ-Fe_5C_2, Nature (2024), https://doi.org/10.1038/s41586-024-08078-5.

[10] X. Han, M. Qing, H. Wang, X. Yu, H. Suo, X. Shen, Y. Yang, Y. Li, Effect of Fe_3O_4 content on the CO_2 selectivity of iron-based catalyst for Fischer–Tropsch synthesis, J. Fuel Chem. Technol. 51 (2023) 155–164, https://doi.org/10.1016/S1872-5813(22)60018-5.

[11] M. Ding, Y. Yang, B. Wu, T. Wang, L. Ma, H. Xiang, Y. Li, Transformation of carbonaceous species and its influence on catalytic performance for iron-based Fischer–Tropsch synthesis catalyst, J. Mol. Catal. A Chem. 351 (2011) 165–173, https://doi.org/10.1016/j.molcata.2011.10.001.

[12] D.V. Peron, A.J. Barrios, A. Taschin, I. Dugulan, C. Marini, G. Gorni, S. Moldovan, S. Koneti, R. Wojcieszak, J.W. Thybaut, M. Virginie, A.Y. Khodakov, Active phases for high temperature Fischer–Tropsch synthesis in the silica supported iron catalysts promoted with antimony and tin, Appl. Catal. B: Environ. 292 (2021), https://doi.org/10.1016/j.apcatb.2021.120141.

[13] Y. Liu, F. Lu, Y. Tang, M. Liu, F.F. Tao, Y. Zhang, Effects of initial crystal structure of Fe_2O_3 and Mn promoter on effective active phase for syngas to light olefins, Appl. Catal. b: Environ., 261 (2020) 118219, https://doi.org/10.1016/j.apcatb.2019.118219.

[14] C. Zhang, Y. Yang, B. Teng, T. Li, H. Zheng, H. Xiang, Y. Li, Study of an iron-manganese Fischer–Tropsch synthesis catalyst promoted with copper, J. Catal. 237 (2006) 405–415, https://doi.org/10.1016/j.jcat.2005.11.004.

[15] V.R.R. Pendyala, U.M. Graham, G. Jacobs, H.H. Hamdeh, B.H. Davis, Fischer–Tropsch synthesis: morphology, phase transformation, and carbon-layer growth of iron-based catalysts, ChemCatChem 6 (2014) 1952–1960, https://doi.org/10.1002/cctc.201402073.

[16] Q. Yang, V.A. Kondratenko, A.S. Skrypnik, H. Lund, S. Bartling, J. Weiss, A. Brückner, E.V. Kondratenko, Understanding of the fate of α-Fe_2O_3 in CO_2 hydrogenation through combined time-resolved in situ characterization and microkinetic analysis, ACS Catal. 13 (2023) 9064–9077, https://doi.org/10.1021/acscatal.3c01340.

[17] J. Chai, R. Pestman, F. Chiang, Z. Men, P. Wang, E.J.M. Hensen, Influence of carbon deposits on Fe-carbide for the Fischer–Tropsch reaction, J. Catal. 416 (2022) 289–300, https://doi.org/10.1016/j.jcat.2022.11.002.

[18] D. Peña, A. Cognigni, T. Neumayer, W. van Beek, D.S. Jones, M. Quijada, M. Ronning, Identification of carbon species on iron-based catalysts during Fischer-Tropsch synthesis, Appl. Catal. A 554 (2018) 10–23, https://doi.org/10.1016/j.apcata.2018.01.019.

[19] A.N. Pour, M.R. Housaindokht, Fischer-Tropsch synthesis on iron catalyst promoted with HZSM-5 zeolite: regeneration studies of catalyst, J. Nat. Gas Sci. Eng. 14 (2013) 49–54, https://doi.org/10.1016/j.jngse.2013.05.004.

[20] J. Gorimbo, X. Lu, X. Liu, Y. Yao, D. Hildebrandt, D. Glasser, Low-pressure Fischer-Tropsch synthesis: in situ oxidative regeneration of iron catalysts, Ind. Eng. Chem. Res. 56 (2017) 4267–4274, https://doi.org/10.1021/acs.iecr.7b00008.

[21] E.T.C. Vogt, D. Fu, B.M. Weckhuysen, Carbon deposit analysis in catalyst deactivation, regeneration, and rejuvenation, Angew. Chem. Int. Ed. 62 (2023), https://doi.org/10.1002/anie.202300319.

[22] T.A. Wezendonk, V.P. Santos, M.A. Nasalevich, Q.S.E. Warringa, A.I. Dugulan, A. Chojecki, A.C.J. Koeken, M. Ruitenbeek, G. Meima, H. Islam, G. Sankar, M. Makkee, F. Kapteijn, J. Gascon, Elucidating the nature of Fe species during pyrolysis of the Fe-BTC MOF into highly active and stable Fischer–Tropsch catalysts, ACS Catal. 6 (2016) 3236–3247, https://doi.org/10.1021/acscatal.6b00426.

[23] Z. Klencsár, Mössbauer spectrum analysis by evolution algorithm, Nucl. Instrum. Methods Phys. Res. B. 129 (1997) 527–533, https://doi.org/10.1016/S0168-583X(97)00314-5.

[24] H. Zhao, J. Liu, C. Yang, S. Yao, H. Su, Z. Gao, M. Dong, J. Wang, A.I. Rykov, J. Wang, Y. Hou, W. Li, D. Ma, Synthesis of iron-carbide nanoparticles: identification of the active phase and mechanism of Fe-based Fischer–Tropsch synthesis, CCS Chem. 3 (2021) 10.31635/ccschem.020.202000555.

[25] K. Xu, B. Sun, J. Lin, W. Wen, Y. Pei, S. Yan, M. Qiao, X. Zhang, B. Zong, ε-Iron carbide as a low-temperature Fischer–Tropsch synthesis catalyst, Nat. Commun. 5 (2014) 5783, https://doi.org/10.1038/ncomms6783.

[26] T.A. Wezendonk, X. Sun, A.I. Dugulan, A.J.F. Van Hoof, E.J.M. Hensen, F. Kapteijn, J. Gascon, Controlled formation of iron carbides and their performance in Fischer–Tropsch synthesis, J. Catal. 362 (2018) 106–117, https://doi.org/10.1016/j.jcat.2018.03.034.

[27] X. Li, K. Zhu, J. Pang, M. Tian, J. Liu, A.I. Rykov, M. Zheng, X. Wang, X. Zhu, Y. Huang, B. Liu, J. Wang, W. Yang, T. Zhang, Unique role of Mössbauer spectroscopy in assessing structural features of heterogeneous catalysts, Appl. Catal. b: Environ., 224 (2018) 518–532, https://doi.org/10.1016/j.apcatb.2017.11.004.

[28] X.W. Liu, S. Zhao, Y. Meng, Q. Peng, A.K. Dearden, C.F. Huo, Y. Yang, Y.W. Li, X. D. Wen, Mossbauer spectroscopy of iron carbides: from prediction to experimental confirmation, Sci. Rep. 6 (2016), https://doi.org/10.1038/srep26184.

[29] G. Raupp, Mössbauer investigation of supported Fe and FeNi catalysts II. Carbides formed Fischer–Tropsch synthesis, J. Catal. 58 (1979) 348–360, https://doi.org/10.1016/0021-9517(79)90274-4.

[30] A. Boubnov, H. Lichtenberg, S. Mangold, J. Grunwaldt, Identification of the iron oxidation state and coordination geometry in iron oxide- and zeolite-based catalysts using pre-edge XAS analysis, J. Synchrotron Rad., 22 (2015) 410–426, https://doi.org/10.1107/S1600577514025880.

[31] Q. Yang, V.A. Kondratenko, S.A. Petrov, D.E. Doronkin, E. Saraci, H. Lund, A. Arinchtein, R. Kraehnert, A.S. Skrypnik, A.A. Matvienko, E.V. Kondratenko, Identifying performance descriptors in CO_2 Hydrogenation over iron-based catalysts promoted with alkali metals, Angew. Chem. Int. Ed. 61 (2022) e202116517, https://doi.org/10.1002/anie.202116517.

[32] L. Guo, J. Sun, X. Ji, J. Wei, Z. Wen, R. Yao, H. Xu, Q. Ge, Directly converting carbon dioxide to linear α-olefins on bio-promoted catalysts, Commun. Chem., 1 (2018), https://doi.org/10.1038/s42004-018-0012-4.

[33] M. Amoyal, R. Vidruk-Nehemya, M.V. Landau, M. Herskowitz, Effect of potassium on the active phases of Fe catalysts for carbon dioxide conversion to liquid fuels through hydrogenation, J. Catal. 348 (2017) 29–39, https://doi.org/10.1016/j.jcat.2017.01.020.

[34] Y.J. Li, Z.S. Li, A. Ahsen, L. Lammich, G.J.A. Mannie, J.W.H. Niemantsverdriet, J. V. Lauritsen, Atomically defined iron carbide surface for Fischer–Tropsch synthesis catalysis, ACS Catal. 9 (2019) 1264–1273, https://doi.org/10.1021/acscatal.8b03684.

[35] D.J. Miller, M.C. Biesinger, N.S. McIntyre, Interactions of CO_2 and CO at fractional atmosphere pressures with iron and iron oxide surfaces: one possible mechanism for surface contamination? Surf. Interface Anal. 33 (2002) 299–305, https://doi.org/10.1002/sia.1188.

[36] A. Furlan, U. Jansson, J. Lu, L. Hultman, M. Magnuson, Structure and bonding in amorphous iron carbide thin films, J. Phys. Condens. Matter 27 (2015) 045002, https://doi.org/10.1088/0953-8984/27/4/045002.

[37] M.D. Shroff, A.K. Datye, The importance of passivation in the study of iron Fischer-Tropsch catalysts, Catal. Lett. 37 (1996) 101–106, https://doi.org/10.1007/BF00813526.

[38] S. Janbroers, J.N. Louwen, H.W. Zandbergen, P.J. Kooyman, Insights into the nature of iron-based Fischer-Tropsch catalysts from quasi in situ TEM-EELS and XRD, J. Catal. 268 (2009) 235–242, https://doi.org/10.1016/j.jcat.2009.09.021.

[39] M.C. Biesinger, Accessing the robustness of adventitious carbon for charge referencing (correction) purposes in XPS analysis: insights from a multi-user facility data review, Appl. Surf. Sci. 597 (2022) 153681, https://doi.org/10.1016/j.apsusc.2022.153681.

[40] X. Chen, X. Wang, D. Fang, A review on C1s XPS-spectra for some kinds of carbon materials, Fuller. Nanotub. Carbon Nanostruct., 28 (2020) 1048–1058, https://doi.org/10.1080/1536383X.2020.1794851.

[41] J. Xu, C.R. Bartholomew, Temperature-programmed hydrogenation (TPH) and in situ Mössbauer spectroscopy studies of carbonaceous species on silica-supported iron Fischer−Tropsch catalysts, J. Phys. Chem. B 109 (2005) 2392–2403, https://doi.org/10.1021/jp048808j.

[42] P. Sirikulbodee, M. Phongaksorn, T. Sornchamni, T. Ratana, S. Tungkamani, Effect of different iron phases of Fe/SiO_2 Catalyst in CO_2 hydrogenation under mild conditions, Catalysts 12 (2022) 698, https://doi.org/10.3390/catal12070698.

[43] Q. Yang, E.A. Fedorova, S.A. Petrov, J. Weiss, H. Lund, A.S. Skrypnik, C. R. Kreyenschulte, V.Y. Bychkov, A.A. Matvienko, A. Brueckner, E.V. Kondratenko, Activity and selectivity descriptors for iron carbides in CO_2 hydrogenation, Appl. Catal. b: Environ., 327 (2023) 122450, https://doi.org/10.1016/j.apcatb.2023.122450.

[44] T.H. Nguyen, H.B. Kim, E.D. Park, CO and CO_2 Methanation over CeO_2-supported cobalt catalysts, Catalysts 12 (2022) 212, https://doi.org/10.3390/catal12020212.

[45] R. Escribano, J.J. Sloan, N. Siddique, N. Sze, T. Dudev, Raman Spectroscopy of carbon-containing particles, Vib. Spectrosc 26 (2001) 179–186, https://doi.org/10.1016/S0924-2031(01)00106-0.

[46] N. Shimodaira, A. Masui, Raman spectroscopic investigations of activated carbon materials, J. Appl. Phys. 92 (2002) 902–909, https://doi.org/10.1063/1.1487434.

[47] Z. Li, L. Deng, I.A. Kinloch, R.J. Young, Raman spectroscopy of carbon materials and their composites: graphene, nanotubes and fibres, Prog. Mater Sci. 135 (2023) 101089, https://doi.org/10.1016/j.pmatsci.2023.101089.

[48] P.P. Paalanen, S.H. van Vreeswijk, B.M. Weckhuysen, Combined in situ X-ray powder Diffractometry/Raman spectroscopy of iron carbide and carbon species evolution in Fe(−Na–S)/α-Al_2O_3 catalysts during Fischer–Tropsch synthesis, ACS Catal. 10 (2020) 9837–9855, https://doi.org/10.1021/acscatal.0c01851.

[49] A. Sadezky, H. Muckenhuber, H. Grothe, R. Niessner, U. Pöschl, Raman microspectroscopy of soot and related carbonaceous materials: spectral analysis

and structural information, Carbon 43 (2005) 1731–1742, https://doi.org/10.1016/j.carbon.2005.02.018.
[50] Y. Wang, D.C. Alsmeyer, R.L. McCreery, Raman spectroscopy of carbon materials: structural basis of observed spectra, Chem. Mater. 2 (1990) 557–563, https://doi.org/10.1021/cm00011a018.
[51] Z. Li, W. Wu, M. Wang, Y. Wang, X. Ma, L. Luo, Y. Chen, K. Fan, Y. Pan, H. Li, J. Zeng, Ambient-pressure hydrogenation of CO_2 into long-chain olefins, Nat. Commun. 13 (2022), https://doi.org/10.1038/s41467-022-29971-5.